Net-proton number fluctuations and the Quantum Chromodynamics critical point

Observations from collisions of heavy-ion at relativistic energies have established the formation of a new phase of matter, Quark Gluon Plasma (QGP), a deconfined state of quarks and gluons [1] in a specific region of the temperature versus baryonic chemical potential phase diagram of strong interactions. A program to study the features of the phase diagram, such as a possible critical point, by varying the collision energy ($\sqrt{s_{\rm NN}}$), is performed at the Relativistic Heavy-Ion Collider (RHIC) facility. Non-monotonic variation with $\sqrt{s_{\rm NN}}$ of moments of the net-baryon number distribution, related to the correlation length and the susceptibilities of the system, is suggested as a signature for a critical point [2–4]. We report the first evidence of a non-monotonic variation in kurtosis $\times$ variance of the net-proton number (proxy for net-baryon number) distribution as a function of $\sqrt{s_{\rm NN}}$ with 3.1σ significance, for head-on (central) gold-on-gold (Au+Au) collisions measured using the STAR detector [5] at RHIC. Non-central Au+Au collisions and models of heavy-ion collisions without a critical point show a monotonic variation as a function of $\sqrt{s_{\rm NN}}$.

One of the fundamental goals in physics is to understand the properties of matter when subjected to variations in temperature and pressure. Currently, the study of the phases of strongly interacting nuclear matter is the focus of many research activities worldwide, both theoretically and experimentally [6,7]. The theory that governs the strong interactions is Quantum Chromodynamics (QCD), and the corresponding phase diagram is called the QCD phase diagram. From

different examples of condensed-matter systems, experimental progress in mapping out phase diagrams is achieved by changing the material doping, adding more holes than electrons. Similarly it is suggested for the QCD phase diagram, that adding more quarks than antiquarks (the energy required is defined by the baryonic chemical potential, μ_B), through changing the heavy-ion collision energy, enables a search for new emergent properties and a critical point in the phase diagram. Figure 1 shows a conjectured QCD phase diagram. It has at least two distinct phases: a QGP at higher temperatures, and a state of confined quarks and gluons at lower temperatures called the hadronic phase [8–10]. It is inferred from lattice QCD calculations [11] that the transition is consistent with being a cross over at small μ_B, and that the transition temperature is about 155 MeV [12–14]. An important predicted feature of the QCD phase structure is a critical point [2,15], followed at higher μ_B by a first order phase transition. Attempts are being made to locate the critical point both experimentally and theoretically. Current theoretical calculations are highly uncertain about the location of the critical point. Lattice QCD calculations at finite μ_B face numerical challenges in computing [16,17]. Within these limitations, the current best estimate from Lattice QCD is that there is a critical point located above $\mu_B \sim 300$ MeV [16,17]. The goal of this work is to search for the possible signatures of the critical point by scanning the temperature (T) versus μ_B in the QCD phase diagram by varying the collision energy $\sqrt{s_{NN}}$ of the heavy-ion collisions [3].

Another key aspect of investigating the QCD phase diagram is to determine whether the system has attained thermal equilibrium. Several theoretical interpretations of experimental data have the underlying assumption that the system produced in the collisions should have come to local thermal equilibrium during its evolution. Experimental tests of thermalization for these femto-

scale expanding systems are non-trivial. However, the yields of produced hadrons and fluctuations of multiplicity distributions related to conserved quantities have been studied and shown to have characteristics of thermodynamic equilibrium for higher collision energies [16,18–23].

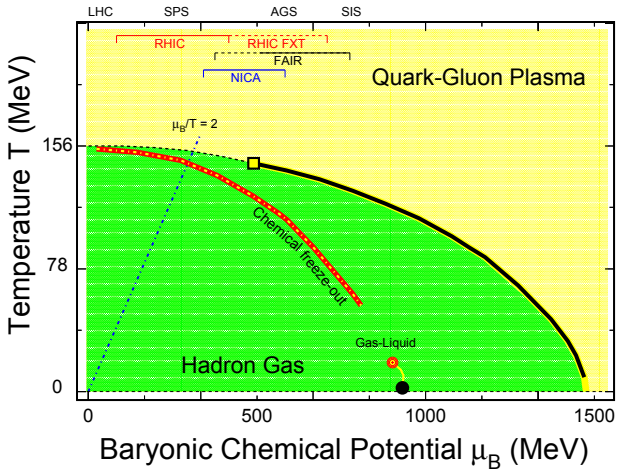

Figure 1: Conjectured QCD phase diagram. The phase boundary (solid line) between the hadronic gas phase and the high-temperature quark-gluon phase is a first-order phase transition line, which begins at large μ_B and small T and curves towards smaller μ_B and larger T. This line ends at the QCD critical point whose conjectured position, indicated by a square, is uncertain both theoretically and experimentally. At smaller μ_B there is a cross over indicated by a dashed line. The region of $\mu_B/T \leq 2$ is shown as blue dot-dashed line. A comparison between RHIC data and lattice QCD calculations disfavors the possible QCD critical point being located at $\mu_B/T \leq 2$ [16,17]. The red-yellow dotted line corresponds to the chemical freeze-out (where inelastic collisions among the constituents of the system cease) inferred from particle yields in heavy-ion collisions using a thermal model. The liquid-gas transition region features a second order critical point (red-circle) and a first-order transition line (yellow line) that connect the critical point to the ground state of nuclear matter ($T \sim 0$ and $\mu_B \sim 925$ MeV) [8]. The regions of the phase diagram accessed by past (AGS and SPS), ongoing (LHC, RHIC, SPS and RHIC operating in fixed target mode), and future (FAIR and NICA) experimental facilities are also indicated.

Upon approaching a critical point, the correlation length diverges and thus renders, to a large extent, microscopic details irrelevant. Hence observables like the moments of the conserved net-baryon number distribution, which are sensitive to the correlation length, are of interest when searching for a critical point. A non-monotonic variation of these moments as a function of $\sqrt{s_{\rm NN}}$ has been proposed as an experimental signature of a critical point [2,3]. However, considering the complexity of the system formed in heavy-ion collisions, signatures of a critical point are detectable only if they can survive the evolution of the system, including the effects of finite size and time [24]. Hence, it was proposed to study higher moments of distributions of conserved quantities (N) due to their stronger dependence on the correlation length [15]. The promising higher moments are the skewness, $S = \left\langle (\delta N)^3 \right\rangle / \sigma^3$, and kurtosis, $\kappa = [\left\langle (\delta N)^4 \right\rangle / \sigma^4] - 3$, where $\delta N = N - M$, M is the mean and σ is the standard deviation. The magnitude and the sign of the moments, which quantify the shape of the multiplicity distributions, are important for understanding the critical point [3,25]. An additional crucial experimental challenge is to reconstruct, on an event-by-event basis, all of the baryons produced within the acceptance of a detector [26–28]. However, theoretical calculations have shown that the proton-number fluctuations can also reflect the baryon-number fluctuations at the critical point [29].

The measurements reported here are from Au+Au collisions recorded by the STAR detector [5] at RHIC from the years 2010 to 2017. The data is presented for $\sqrt{s_{\rm NN}}$ = 7.7, 11.5, 14.5, 19.6, 27, 39, 54.4, 62.4 and 200 GeV as part of phase-I of the Beam Energy Scan (BES) program at RHIC [18]. These $\sqrt{s_{\rm NN}}$ values correspond to $\mu_{\rm B}$ values ranging from 420 MeV to 20 MeV at chemical freeze-out [18]. All valid Au+Au collisions occurring within 60 cm (80 cm for $\sqrt{s_{\rm NN}}$ =

7.7 GeV) of the nominal interaction point, having vertex position in the transverse plane within 2 cm (1 cm for $\sqrt{s_{\rm NN}}$ = 14.5 GeV) of the beam axis, and having signals in trigger detectors above a noise threshold (called minimum bias) are included in the analysis [18]. For the results presented here, the number of minimum bias Au+Au collisions ranges between 3 million for $\sqrt{s_{\rm NN}}$ = 7.7 GeV and 585 million at $\sqrt{s_{\rm NN}}$ = 54.4 GeV. These statistics are found to be sufficient in order to compute the moments of the net-proton distributions up to the fourth order [30]. The collisions are further characterised by their impact parameter, which is indirectly determined from the measured multiplicity of charged particles other than protons and anti-protons in the pseudo-rapidity range $|\eta| < 1$, where $\eta = -\ln[\tan(\theta/2)]$, with θ being the angle between the momentum of the particle and the positive direction of the beam axis. We exclude protons and anti-protons specifically to avoid self-correlation effects [31]. The effect of self-correlation is found to be negligible from a study carried out using standard heavy-ion collision event generators, HIJING [32] and UrQMD [33]. The effect of resonance decays and the pseudo-rapidity range for centrality determination have been understood and optimised using model calculations [34,35]. The results presented here correspond to two event classes: central collisions (impact parameters $\sim$ 0-3 fm, obtained from the top 5% of the above-mentioned multiplicity distribution) and peripheral collisions (impact parameters $\sim$ 12-13 fm, obtained from the 70-80% region of the multiplicity distribution). The number of events for the top 5% central collisions ranges between 0.14 million for $\sqrt{s_{\rm NN}}$ = 7.7 GeV and 33 million at $\sqrt{s_{\rm NN}}$ = 54.4 GeV.

The protons (p) and anti-protons ($\bar{p}$) are identified, along with their momentum, by reconstructing their tracks in the Time Projection Chamber (TPC) placed within a solenoidal magnetic

field of 0.5 Tesla, and by measuring their ionization energy loss (dE/dx) in the sensitive gas-filled volume of the chamber. The selected kinematic region for protons covers all azimuthal angles for the rapidity range $|y| < 0.5$, where rapidity is the arctanh of the component of speed parallel to the beam direction in units of the speed of light, with full azimuthal angle. The precise measurement of dE/dx with a resolution of 7% in Au+Au collisions allows for a clear identification of protons up to 800 MeV/c in transverse momentum (p_{T}, the component of momentum perpendicular to the beam direction). The identification for larger p_{T} (up to 2 GeV/c, with purity above 97%) was made by a Time Of Flight detector (TOF) (see Methods) having a timing resolution of better than 100 ps. A minimum p_{T} threshold of 400 MeV/c and a maximum distance of closest approach to the collision vertex of 1 cm for each $p(\bar{p})$ candidate track is used to suppress contamination from secondaries (for example protons from interactions of energetic particles produced in the collisions with detector materials) [18,36]. This p_{T} acceptance accounts for approximately 80% of the total p + $\bar{p}$ multiplicity at mid-rapidity. This is a significant improvement from the results previously reported [36] which only had the $p + \bar{p}$ measured using the TPC ($0.4 < p_{\mathrm{T}}$ (GeV/c) < 0.8), whereas the current analysis includes the addition of the TOF detector, where the p_{T} acceptance is increased up to 2 GeV/c. The observation of non-monotonic variation of the kurtosis $\times$ variance is much more significant with the increased acceptance. The increased fluctuations are found to have contributions from protons and anti-protons in the entire p_{T} range studied. For the rapidity dependence of the observable see Fig. 7 in Methods.

Figure 2 shows the event-by-event net-proton ($N_p - N_{\bar{p}} = \Delta N_p$) distributions obtained by measuring the number of protons (N_p) and anti-protons ($N_{\bar{p}}$) at mid-rapidity ($|y| < 0.5$) in the

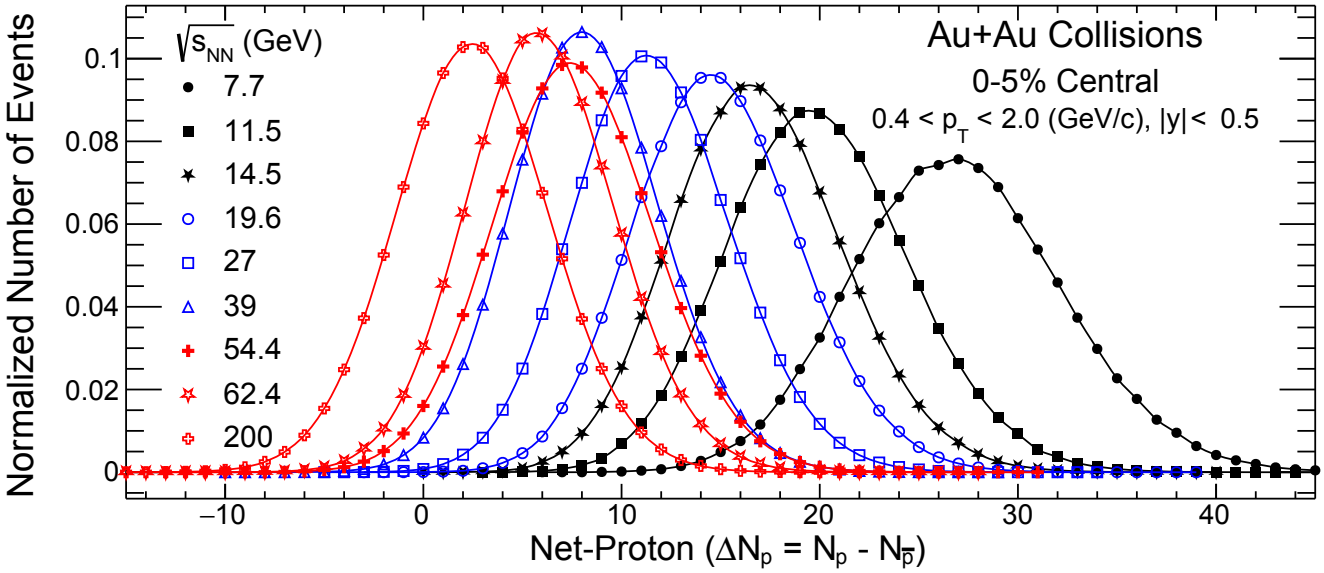

Figure 2: Event-by-event net-proton number distributions for head-on (0-5% central) Au+Au collisions for nine $\sqrt{s_{\rm NN}}$ values measured by the STAR detector at RHIC. The distributions are normalized to the total number of events at each $\sqrt{s_{\rm NN}}$. The statistical uncertainties are smaller than the symbol sizes and the lines are to guide the eye. The distributions in this figure are not corrected for proton and anti-proton detection efficiency. The deviation of the distribution for $\sqrt{s_{\rm NN}}$ = 54.4 GeV from the general energy dependence trend is understood to be due to the reconstruction efficiency of protons and anti-protons being different compared to other energies.

transverse momentum range $0.4 < p_{\rm T}$ (GeV/c)< 2.0 for Au+Au collisions at various $\sqrt{s_{\rm NN}}$. To study the shape of the event-by-event net-proton distribution in detail, cumulants (C_n) of various orders are calculated, where $C_1 = M$, $C_2 = \sigma^2$, $C_3 = S\sigma^3$ and $C_4 = \kappa\sigma^4$.

Figure 3 shows the variation of net-proton cumulants (C_n) as a function of $\sqrt{s_{\rm NN}}$ for central and peripheral Au+Au collisions. The cumulants are corrected for the multiplicity variations

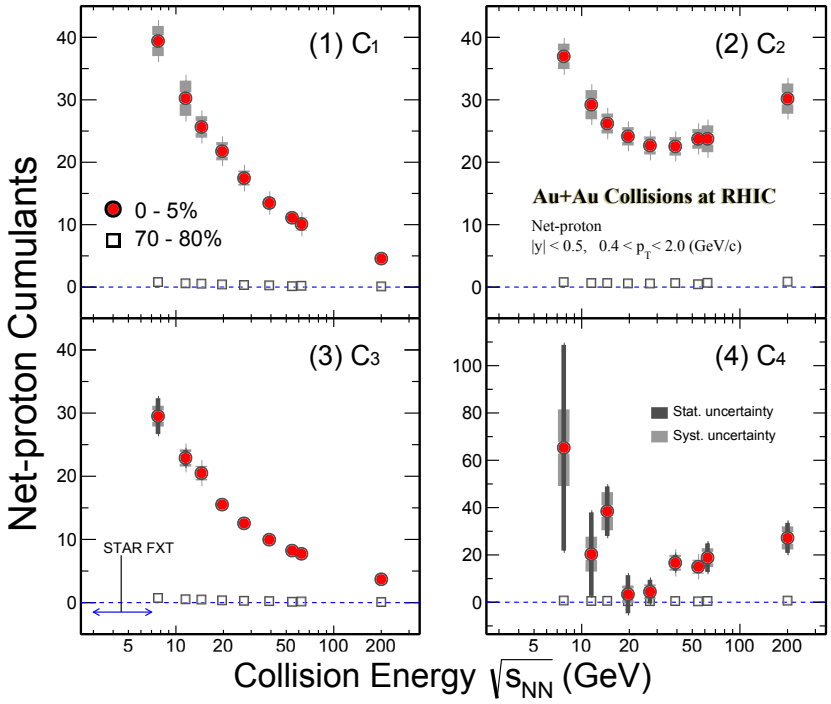

Figure 3: Cumulants (C_n) of the net-proton distributions for central (0-5%) and peripheral (70-80%) Au+Au collisions as a function of collision energy. The transverse momentum (p_{T}) range for the measurements is from 0.4 to 2 GeV/c and the rapidity (y) range is $\pm$ 0.5. The vertical narrow and wide bars represent the statistical uncertainties and systematic uncertainties, respectively. The energy range for the STAR fixed-target (FXT) program is shown as arrows in panel (3).

arising due to finite impact parameter range for the measurements [34]. These corrections suppress the volume fluctuations considerably [34,37]. A different volume fluctuation correction method [38] has been applied to the 0-5% central Au+Au collision data and the results were found to be consistent. The cumulants are also corrected for finite track reconstruction efficiencies of the TPC and TOF

detectors. This is done by assuming a binomial probability distribution to reconstruct particles out of those produced [36,39]. A cross-check using a different method based on unfolding (see Methods) of the distributions for central Au+Au collisions at $\sqrt{s_{\rm NN}}$ = 200 GeV has been found to give values consistent with the cumulants shown in Fig. 3. Further, the efficiency correction method used has been verified in a Monte Carlo closure test. Typical values for the efficiencies in the TPC (TOF) for the momentum range studied in 0-5% central Au+Au collisions at $\sqrt{s_{\rm NN}}$ = 7.7 GeV are 83%(72%) and 81%(70%) for the protons and anti-protons, respectively. The corresponding efficiencies for $\sqrt{s_{\rm NN}}$ = 200 GeV collisions are 62%(69%) and 60%(68%) for the protons and anti-protons, respectively. The statistical uncertainties are obtained using both a bootstrap approach [30,39] and the Delta theorem [30,39,40] method. The systematic uncertainties are estimated by varying the experimental requirements to reconstruct p ($\bar{p}$) in the TPC and TOF. These requirements include the distance of the proton and anti-proton tracks from the primary vertex position, track quality reflected by the number of TPC space points used in the track reconstruction, the particle identification criteria, and the uncertainties in estimating the reconstruction efficiencies. The systematic uncertainties at different collision energies are uncorrelated.

The large values of C_3 and C_4 for central Au+Au collisions show that the distributions have non-Gaussian shapes[‡], a first possible indication of enhanced fluctuations arising from a possible critical point [15,25]. The corresponding values for peripheral collisions are small and close to zero. For central collisions, the C_1 and C_3 monotonically decrease with $\sqrt{s_{\rm NN}}$, while the C_2 and C_4 show a non-monotonic variation, with a possible minimum between $\sqrt{s_{\rm NN}}$ of 11.5 and 39 GeV.

[‡]Data in Fig. 4 shows deviation from a Skellam expectation.

We employ ratios of cumulants in order to cancel volume variations to first order. Further, these ratios of cumulants are related to the ratio of baryon-number susceptibilities ($\chi_n^{\rm B} = \frac{d^n P}{d\mu_B^n}$, where n is the order and P is the pressure of the system) at a given T and $\mu_{\rm B}$, computed in QCD and QCD-based models [4] as: $C_3/C_2 = S\sigma = (\chi_3^{\rm B}/T)/(\chi_2^{\rm B}/T^2)$ and $C_4/C_2 = \kappa\sigma^2 = (\chi_4^{\rm B})/(\chi_2^{\rm B}/T^2)$. Close to the critical point, QCD-based calculations predict the net-baryon number distributions to be non-Gaussian and susceptibilities to diverge, causing moments, especially higher-order quantities like $\kappa\sigma^2$, to have non-monotonic variation as a function of $\sqrt{s_{\rm NN}}$ [4,41].

Figure 4 shows the variation of $S\sigma$ (or C_3/C_2) and $\kappa\sigma^2$ (or C_4/C_2) as a function of $\sqrt{s_{\rm NN}}$ for central and peripheral Au+Au collisions. In central collisions a non-monotonic variation with beam energy is observed for $\kappa\sigma^2$. The $\kappa\sigma^2$ values go below unity (statistical baseline) and then rise towards values above unity with decrease in beam energy. The peripheral collisions on the other hand show a monotonic variation with $\sqrt{s_{\rm NN}}$ and $\kappa\sigma^2$ values are always below unity. It is worth noting that in peripheral collisions, the system formed may not be hot and dense enough to undergo a phase transition or come close to the QCD critical point. The central Au+Au collision data for $\kappa\sigma^2$ ($S\sigma$), in the collision energy range of 7.7 – 62.4 GeV, are well described by a polynomial function of order four (five) in $\sqrt{s_{\rm NN}}$, with χ^2/NDF $\sim$ 1.3(0.72). The derivative of the polynomial function changes sign (see Methods) with $\sqrt{s_{\rm NN}}$ thereby indicating a non-monotonic variation of the measurement with the collision energy. The uncertainties of the derivatives are obtained by varying the data points randomly at each energy within the statistical and systematic uncertainties separately. The overall significance of the change in the sign of the slope for C_4/C_2 versus $\sqrt{s_{\rm NN}}$, based on the fourth order polynomial function fitting procedure, from $\sqrt{s_{\rm NN}}$ = 7.7 to 62.4 GeV is

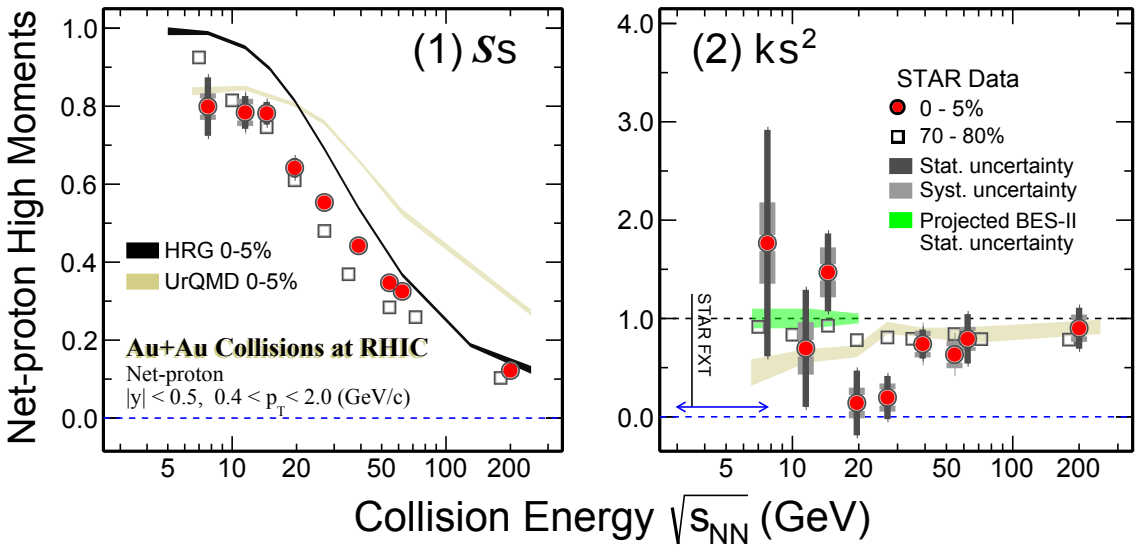

Figure 4: $S\sigma$ (1) and $\kappa\sigma^2$ (2) as a function of collision energy for net-proton distributions measured in Au+Au collisions. The results are shown for central (0-5%, filled circles) and peripheral (70-80%, open squares) collisions within $0.4 < p_{\rm T}$ (GeV/c) < 2.0 and $|y| < 0.5$. The vertical narrow and wide bars represent the statistical and systematic uncertainties, respectively. Shaded green band is the estimated statistical uncertainty for BES-II and the energy range for STAR fixed-target (FXT) program is shown as arrows in panel (2). The peripheral data points have been shifted along x-axis for clarity of presentation. Results from a hadron resonance gas (HRG) model [35] and a transport model calculation (UrQMD [33]) for central collisions (0-5%) are shown as black and gold bands, respectively. These model calculations utilize the experimental acceptance, and incorporate conservation laws for strong interactions, but do not include a phase transition or a critical point.

3.1σ. This significance is obtained by generating one million sets of points, where for each set, the measured C_4/C_2 value at a given $\sqrt{s_{\rm NN}}$ is randomly varied within the total Gaussian uncertainties (systematic and statistical uncertainties added in quadrature). Then for each new C_4/C_2 versus

$\sqrt{s_{\rm NN}}$ set of points, a fourth order polynomial function is fitted and the derivative values calculated at different $\sqrt{s_{\rm NN}}$ (as discussed above). Out of the one million set of points, 1143 are found to have the same derivative sign at all $\sqrt{s_{\rm NN}}$. The probability that at least one derivative at a given $\sqrt{s_{\rm NN}}$ has a different sign from the remaining ones in the one million set of points is found to be 0.998857, which corresponds to 3.1σ. The significances are calculated using statistical and systematic uncertainties of the derivatives, added in quadrature.

The expectations from an ideal statistical model of hadrons assuming thermodynamical equilibrium, called the Hadron Resonance Gas (HRG) model [35], calculated within the experimental acceptance, are also shown in Fig. 4. The HRG results are similar to those from a system of totally uncorrelated and statistically random particle production. The HRG results are close to unity for $\kappa\sigma^2$ without any dependence on $\sqrt{s_{\rm NN}}$. For $S\sigma$, HRG calculations deviate significantly from measurements for Au+Au collisions at 0-5% centrality below $\sqrt{s_{\rm NN}}$ = 62.4 GeV. Corresponding $\kappa\sigma^2$ ($S\sigma$) results for 0-5% Au+Au collisions from a transport-based UrQMD model [33] calculation, which incorporates conservation laws and most of the relevant physics apart from a phase transition or a critical point, and which is calculated within the experimental acceptance, show a monotonic decrease (increase) with decreasing collision energy. Similar conclusions are obtained from JAM [42], another microscopic transport model. Neither of the model calculations explains the measured dependence of the $\kappa\sigma^2$ and $S\sigma$ of the net-proton distribution on $\sqrt{s_{\rm NN}}$ for central Au+Au collisions.

In conclusion, we have presented measurements of net-proton cumulant ratios with the STAR

detector at RHIC over a wide range in μ_B (20 to 420 MeV) which are relevant to a QCD critical point search in the QCD phase diagram. We have observed a non-monotonic behaviour, as a function of $\sqrt{s_{NN}}$, in net-proton $\kappa\sigma^2$ in central Au+Au collisions with a significance of 3.1σ. In contrast, monotonic behaviour with $\sqrt{s_{NN}}$ is observed for the statistical hadron gas model, and for a nuclear transport model without a critical point, as observed experimentally in peripheral collisions. The deviation of the measured $\kappa\sigma^2$ from several baseline calculations with no critical point, and its non-monotonic dependence on $\sqrt{s_{NN}}$, are qualitatively consistent with expectations from a QCD-based model which includes a critical point [3,15]. Our measurements can also be compared to the baryon-number susceptibilities computed from QCD to understand various other features of the QCD phase structure as well as to obtain the freeze-out conditions in heavy-ion collisions. Higher event statistics, which will allow for a more differential measurement of these experimental observables in y-p_T along with comparison to theoretical QCD calculations which includes the dynamics associated with heavy-ion collisions, will help in establishing the critical point.

Acknowledgements We thank P. Braun-Munzinger, S. Gupta, F. Karsch, M. Kitazawa, V. Koch, D. Mishra, K. Rajagopal, K. Redlich, and M. Stephanov for several stimulating discussions. We thank the RHIC Operations Group and RCF at BNL, the NERSC Center at LBNL, and the Open Science Grid consortium for providing resources and support. This work was supported in part by the Office of Nuclear Physics within the U.S. DOE Office of Science, the U.S. National Science Foundation, the Ministry of Education and Science of the Russian Federation, National Natural Science Foundation of China, Chinese Academy of Science, the Ministry of Science and Tech-

nology of China and the Chinese Ministry of Education, the Higher Education Sprout Project by Ministry of Education at NCKU, the National Research Foundation of Korea, Czech Science Foundation and Ministry of Education, Youth and Sports of the Czech Republic, Hungarian National Research, Development and Innovation Office, New National Excellency Programme of the Hungarian Ministry of Human Capacities, Department of Atomic Energy and Department of Science and Technology of the Government of India, the National Science Centre of Poland, the Ministry of Science, Education and Sports of the Republic of Croatia, RosAtom of Russia and German Bundesministerium fur Bildung, Wissenschaft, Forschung and Technologie (BMBF), Helmholtz Association, Ministry of Education, Culture, Sports, Science, and Technology (MEXT) and Japan Society for the Promotion of Science (JSPS).

1. Shuryak, E.V., Quantum Chromodynamics and the Theory of Superdense Matter, *Phys. Rept.* **61**, 71 (1980).

2. Stephanov, M.A., Rajagopal, K., and Shuryak, E.V., Event-by-event fluctuations in heavy ion collisions and the QCD critical point, *Phys. Rev.* **D60**, 114028 (1999).

3. Stephanov, M.A., On the Sign of kurtosis near the QCD critical point, *Phys. Rev. Lett.* **107**, 052301 (2011).

4. Gavai, R.V., and Gupta, S., Lattice QCD predictions for shapes of event distributions along the freezeout curve in heavy-ion collisions, *Phys. Lett.* **B696**, 459 (2011).

5. Ackermann, K. H. *et al.*, STAR detector overview, *Nucl. Instrum. Meth.* **A499**, 624 (2003).

6. Bzdak, A.,Esumi, S.,Koch, V.,Liao, J.,Stephanov, M. and Xu, N., Mapping the Phases of Quantum Chromodynamics with Beam Energy Scan, *arXiv:1906.00936 [nucl-th]*.

7. Luo, X., Xu, N., Search for the QCD Critical Point with Fluctuations of Conserved Quantities in Relativistic Heavy-Ion Collisions at RHIC : An Overview, *Nucl. Sci. Tech.* **28**, 112 (2017).

8. Fukushima, K. and Hatsuda, T., The phase diagram of dense QCD, *Rept. Prog. Phys.* **74**, 014001 (2011).

9. Braun-Munzinger, P. and Wambach, J., Phase Diagram of Strongly Interacting Matter, *Rev. Mod. Phys.* **81**, 1031 (2009).

10. Asakawa, M. and Yazaki, K., Chiral Restoration at Finite Density and Temperature, *Nucl. Phys.* **A504**, 668 (1989).

11. Aoki, Y., Endrodi, G., Fodor, Z., Katz, S.D. and Szabo, K.K., The Order of the quantum chromodynamics transition predicted by the standard model of particle physics, *Nature* **443**, 675 (2006).

12. Aoki, Y., Borsanyi, S., Durr, S., Fodor, Z., Katz, S.D., Krieg, S., and Szabo, K.K., The QCD transition temperature: results with physical masses in the continuum limit II., *JHEP* **06**, 088 (2009).

13. Bazavov, A. *et al.* Chiral and deconfinement aspects of the QCD transition, *Phys. Rev.* **D85**, 054503 (2012).

14. Gupta, S., Luo, X., Mohanty, B., Ritter, H.G., and Xu, N., Scale for the Phase Diagram of Quantum Chromodynamics, *Science* **332**, 1525 (2011).

15. Stephanov, M.A., Non-Gaussian fluctuations near the QCD critical point, *Phys. Rev. Lett.* **102**, 032301 (2009).

16. Bazavov, A. *et al.*, Skewness and kurtosis of net baryon-number distributions at small values of the baryon chemical potential, *Phys. Rev.* **D96**, 074510 (2017).

17. Bazavov, A. *et al.*, QCD Equation of State to $O(\mu_B^6)$ from Lattice QCD, *Phys. Rev.* **D95**, 054504 (2017).

18. Adamczyk, L. *et al.*, Bulk Properties of the Medium Produced in Relativistic Heavy-Ion Collisions from the Beam Energy Scan Program, *Phys. Rev.* **C96**, 044904 (2017).

19. Andronic, A., Braun-Munzinger, P., Redlich, K. and Stachel, J., Decoding the phase structure of QCD via particle production at high energy, *Nature* **561**, 321 (2018).

20. Almasi, G. A., Friman, B. and Redlich, K., Baryon number fluctuations in chiral effective models and their phenomenological implications, *Phys. Rev.* **D96**, 014027 (2017).

21. Bazavov, A.*et al.*, Freeze-out Conditions in Heavy Ion Collisions from QCD Thermodynamics, *Phys. Rev. Lett.* **109**, 192302 (2012).

22. Borsanyi, S., Fodor, Z., Katz, S. D., Krieg, S., Ratti, C. and Szabo, K. K. Freeze-out parameters from electric charge and baryon number fluctuations: is there consistency?, *Phys. Rev. Lett.* **113**, 052301 (2014).

23. Gupta, S., Mallick, D., Mishra, D. K.,Mohanty, B. and Xu, N., Freeze-out and thermalization in relativistic heavy ion collisions, *arXiv:2004.04681 [hep-ph]*.

24. Berdnikov, B. and Rajagopal, K., Slowing out of equilibrium near the QCD critical point, *Phys. Rev.* **D61**, 105017 (2000).

25. Asakawa, M., Ejiri, S., and Kitazawa, M., Third moments of conserved charges as probes of QCD phase structure, *Phys. Rev. Lett.* **103**, 262301 (2009).

26. Kitazawa, M. and Asakawa, M., Relation between baryon number fluctuations and experimentally observed proton number fluctuations in relativistic heavy ion collisions, *Phys. Rev.* **C86**, 024904 (2012).

27. Bzdak, A. and Koch, V., Acceptance corrections to net baryon and net charge cumulants, *Phys. Rev.* **C86**, 044904 (2012).

28. Bzdak, A., Koch, V. and Skokov, V., Baryon number conservation and the cumulants of the net proton distribution., *Phys. Rev.* **C87**, 014901 (2013).

29. Hatta, Y., and Stephanov, M.A., Proton-number fluctuation as a signal of the QCD critical end point, *Phys. Rev. Lett.* **91**, 102003 (2003).

30. Pandav, A., Mallick, D., and Mohanty, B., Effect of limited statistics on higher order cumulants measurement in heavy-ion collision experiments, *Nucl. Phys.* **A991**, 121608 (2019).

31. Chatterjee, A., Zhang, Y., Zeng, J., Sahoo N.R., Luo, X., Centrality selection effect on higher order cumulants of net-proton multiplicity distributions in relativistic heavy-ion collisions, *Phys. Rev.* **C101**, 034902 (2020).

32. Wang, X.N. and Gyulassy, M., HIJING: A Monte Carlo model for multiple jet production in p p, p A and A A collisions, *Phys. Rev.* **D44**, 3501 (1999).

33. Bleicher, M. *et al.*, Relativistic hadron-hadron collisions in the ultrarelativistic quantum molecular dynamics model, *J. Phys.* **G25**, 1859 (1991).

34. Luo, X., Xu, J., Mohanty, B., and Xu, N., Volume fluctuation and auto-correlation effects in the moment analysis of net-proton multiplicity distributions in heavy-ion collisions, *J. Phys.* **G40**, 105104 (2013).

35. Garg, P., Mishra, D.K., Netrakanti, P.K., Mohanty, B., Mohanty, A.K., Singh, B.K., and Xu, N., Conserved number fluctuations in a hadron resonance gas model, *Phys. Lett.* **B726**, 691 (2013).

36. Adamczyk, L. *et al.*, Energy Dependence of Moments of Net-proton Multiplicity Distributions at RHIC, *Phys. Rev. Lett.* **112**, 032302 (2014).

37. Sugiura, T., Nonaka, T., and Esumi, S., Volume fluctuation and multiplicity correlation in higher-order cumulants, *Phys. Rev.* **C100**, 044904 (2019),

38. Braun-Munzinger, P., Rustamov, A., and Stachel, J., Bridging the gap between event-by-event fluctuation measurements and theory predictions in relativistic nuclear collisions, *Nucl. Phys.* **A960**, 114 (2017),

39. Luo, X., Unified description of efficiency correction and error estimation for moments of conserved quantities in heavy-ion collisions, *Phys. Rev.* **C91**, 034907 (2015).

40. Luo, X., Error Estimation for Moments Analysis in Heavy Ion Collision Experiment, *J. Phys.* **G39**, 025008 (2012).

41. Stokic, B., Friman, B., and Redlich, K., Kurtosis and compressibility near the chiral phase transition, *Phys. Lett.* **B673**, 192 (2009).

42. Zhang, Y., He, S., Liu, H., Yang, Z. and Luo, X., Effects of resonance weak decays and hadronic re-scattering on the proton number fluctuations in Au + Au collisions at $\sqrt{s_{\rm NN}} = 5$ GeV from JAM model, *Phys. Rev.* **C101**, 034909 (2020).

Methods

(a) Event selection and Proton and anti-proton identification in STAR detector:

To reject pile-up and other background events, information from the fast detectors, scintillator based vertex postion detector (VPD) [1] and the time-of-flight (TOF) detector [1,2] and the time projection chamber (TPC) [3] are used. To further ensure a good quality of data, run (a set of minimum bias data taken in a certain time interval) by run study of several variables were carried out to remove bad events. The variables used includes the total number of uncorrected charged particles, average transverse momentum in an event, mean pseudorapidity and azimuthal angle in an event etc. In addition, the distance of closest approach (DCA) of the charged particle track from the primary vertex, especially the signed transverse average DCA and its stability, are studied to remove

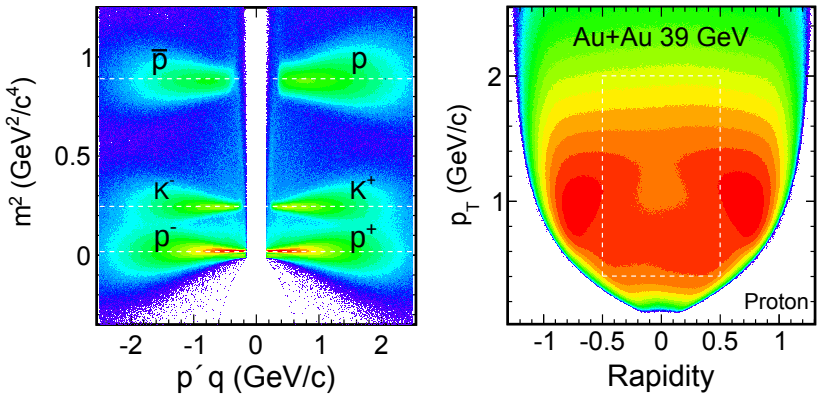

Figure 5: Left panel: Square of the mass of the charged particles, requiring timing information from the TOF, as a function of the product of the momentum (p) and the ratio of the particles charge to the elementary charge e (q), both measured using the TPC in Au+Au collisions at $\sqrt{s_{\rm NN}}$ = 39 GeV. The white dashed lines correspond to the expected square of the mass of each particle species. Right panel: The transverse momentum ($p_{\rm T}$) versus the rapidity (y) for protons measured in the STAR detector for Au+Au collisions.

the bad events. These classes of bad events are primarily related to the unstable beam conditions during the data taking and improper space-charge calibration of TPC.

Figure 5 (left panel) shows a typical distribution of the square of the mass associated with each track in an event obtained from the TOF [1,2] as a function of the product of the momentum and the charge of the track determined by the TPC [3]. The proton candidates are well separated from other hadrons like kaons and pions. The right panel of Fig. 5 shows $p_{\rm T}$ versus y for protons in the STAR detector. The white dashed rectangular box is the region selected for the results presented here. It may be noted that STAR, being a collider experiment, has a $p_{\rm T}$ versus y acceptance near

mid-rapidity that is uniform across all beam energies studied. Uniform acceptance allows for the results to be directly compared across all the $\sqrt{s_{\rm NN}}$.

The constant $p_{\rm T}$ versus y acceptance near mid-rapidity raises the issue of contribution of background protons to the analysis. This can be gauged by looking at the DCA of the proton track from the primary vertex and comparing it to the corresponding results for the anti-protons. A DCA criterion of less than 1 cm is used in the analysis reported here. This criterion reduces the background protons contributions in the momentum range of the study to less than 2-3%. This small effect across all beam energies is added to the systematic uncertainties obtained by varying the DCA criteria between 1.2 and 0.8 cm.

(b) Efficiency corrections using unfolding of net-proton multiplicity distributions:

The unfolding method [4] was applied to a data set that provides the most dense charged particle environment in the detectors (0-5% central Au+Au collisions at $\sqrt{s_{\rm NN}}$ = 200 GeV), where one expects the maximum non-binomial detector effects. Detector-response matrices were determined based on detector simulations with respect to generated and measured protons and anti-protons [5]. All possible non-binomial effects, including multiplicity dependent efficiency, were corrected by utilizing the response matrices. The detector response in such cases was found to be best described by a beta-binomial distribution. Even in this situation, the differences in the binomial [6] and unfolding methods of efficiency correction were at a level of less than one σ of the uncertainties.

Cumulants and their ratios up to the fourth order, corrected for the detector efficiencies using

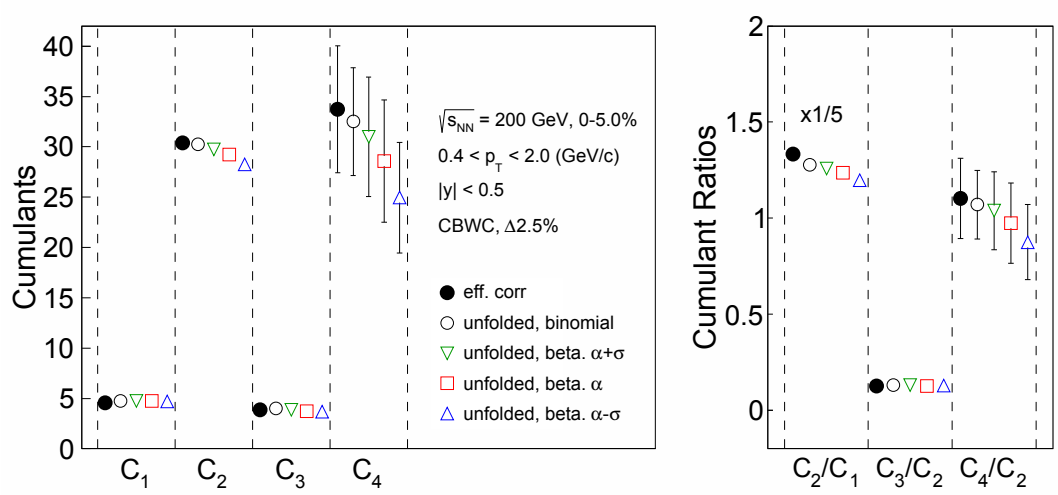

Figure 6: Cumulants and their ratios up to the fourth order, corrected for proton and anti-proton reconstruction efficiencies in $\sqrt{s_{\rm NN}}$ = 200 GeV Au+Au collisions at 0-5% centrality. Results from the conventional efficiency correction are shown as black filled circles, results from the unfolding with the binomial detector response are shown as black open circles, and results from beta-binomial detector response with $\alpha+\sigma$, α and $\alpha-\sigma$ are shown as green triangles, red squares and blue triangles, respectively. The parameter α quantifies the deviation from binomial effects, obtained from simulation. C_2/C_1 is scaled by a constant factor.

the unfolding method, are shown in Fig. 6 for 0-5% central Au+Au collisions at $\sqrt{s_{\rm NN}}$ = 200 GeV. The results are obtained by using centrality bin width correction (CBWC) [34] at 2.5% bin width. For each column, the first point is efficiency corrected using the binomial model method (as employed in the present analysis), the next point is the result corrected for the binomial detector response using the unfolding technique, and the last three points are from unfolding using the beta-binomial response with three values of the non-binomial parameter. The results are ordered from left to right in terms of increasing deviations of the response function compared to the binomial distribution. Checks using unfolding of the distributions for central Au+Au collisions have been found to yield values consistent with the cumulants obtained using the default binomial method of efficiency correction, within the current statistics of the measurements. An alternate approach called the moment expansion method [6] was used for efficiency correction and found to be consistent with the unfolding method.

(c) Rapidity dependence of C_4/C_2 for 0-5% central Au+Au collisions:

The cumulant ratio C_4/C_2 of net-proton multiplicity distributions for 0-5% central Au+Au collisions at $\sqrt{s_{\rm NN}}$ = 7.7, 11.5, 14.5, 19.6, 27, 39, 54.4, 62.4, and 200 GeV is shown in Fig. 7. The C_4/C_2 value is close to unity for all collision energies for the smallest rapidity acceptance. At $\sqrt{s_{\rm NN}}$ = 200 GeV, the C_4/C_2 values remain close to unity as rapidity acceptance is increased, while for $\sqrt{s_{\rm NN}}$ = 7.7 GeV, the C_4/C_2 values increase as rapidity acceptance is increased. The C_4/C_2 values decrease as rapidity acceptance is increased at the intermediate collision energies of $\sqrt{s_{\rm NN}}$ = 19.6 and 27 GeV.

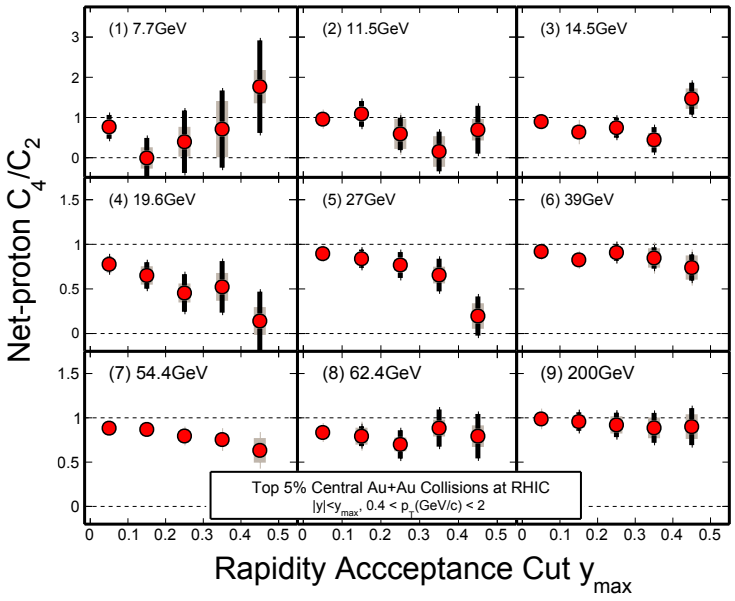

Figure 7: Rapidity dependence of cumulant ratio C_4/C_2 of net-proton multiplicity distributions for 0-5% central Au+Au collisions at $\sqrt{s_{\rm NN}}$ = 7.7, 11.5, 14.5, 19.6, 27, 39, 54.4, 62.4, and 200 GeV. The measurements are done for the p_T range of 0.4 to 2.0 GeV/c. The lines and shaded areas represent statistical and systematic uncertainties.

(d) Values of polynomial function fit to $\kappa\sigma^2$ and $S\sigma$ and their derivatives versus $\sqrt{s_{NN}}$:

The values of the parameters of the polynomial functions for $\kappa\sigma^2$ and $S\sigma$ at $\sqrt{s_{NN}}$ = 7.7, 11.5, 14.5, 19.6, 27, 39, 54.4 and 62.4 GeV are given in Table 1. The uncertainties on the parameters are from the fitting procedure taking into account both the statistical and systematic uncertainties on the data. The χ^2/NDF = 1.3 for the fourth order polynomial fit to $\kappa\sigma^2$ versus $\sqrt{s_{NN}}$ and the χ^2/NDF = 0.72 for the fifth order polynomial fit to $S\sigma$ versus $\sqrt{s_{NN}}$. The $\sqrt{s_{NN}}$ = 200 GeV data point is not included to quantify the non-monotonic variations as the polynomial function fits either did not converge or yielded larger χ^2 values. It may also be noted that the possible critical point is predicted to exist at baryon chemical potential values much larger than those corresponding to $\sqrt{s_{NN}}$ = 200 GeV.

The values of the derivatives of the polynomial functions for $\kappa\sigma^2$ and $S\sigma$ at $\sqrt{s_{NN}}$ = 7.7, 11.5, 14.5, 19.6, 27, 39, 54.4 and 62.4 GeV are given in Table 2. The uncertainties on the derivatives are obtained by varying the data points randomly at each energy within the statistical and systematic uncertainties separately. This process assumes that the systematic uncertainties on the data points are fully uncorrelated. In addition, we also provide an estimate of systematic uncertainty on the derivative at each $\sqrt{s_{NN}}$ which assumes the systematic uncertainties on the data points to be fully correlated. The statistical uncertainties on the derivative values are obtained by the random sampling of the data points using a Gaussian distribution whose mean is the $\kappa\sigma^2$ or $S\sigma$ value of the data and the width of the Gaussian is the statistical uncertainty, respectively, for the data point at each collision energy. The uncorrelated systematic uncertainties are obtained in the same way.

Table 1: Values of the parameters of fourth (fifth) order polynomial that describes the collision energy dependence of $\kappa\sigma^2$ ($S\sigma$) at various $\sqrt{s_{\rm NN}}$ along with their uncertainties. The polynomials are of the form $\sum_n p_n(\sqrt{s_{\rm NN}})^n$, n = 0-4 for fourth order polynomial and 0-5 for fifth order polynomial and p_n are the parameters.

Parameters	$\kappa\sigma^2$	$S\sigma$
p_0	6.24 $\pm$ 1.78	0.51 $\pm$ 0.46
p_1	–0.72 $\pm$ 0.22	0.08 $\pm$ 0.09
p_2	0.03$\pm$0.01	–0.007$\pm$ 0.006
p_3	–0.0005$\pm$0.0002	0.0002 $\pm$ 0.0002
p_4	0.000003 $\pm$ 0.000001	$-3.3\times10^{-6} \pm 2.7\times10^{-6}$
p_5	–	$1.8\times10^{-8} \pm 1.5\times10^{-8}$

Table 2: Values of the derivative of the fourth (fifth) order polynomial that describes the collision energy dependence of $\kappa\sigma^2$ ($S\sigma$) at various $\sqrt{s_{\rm NN}}$. The first uncertainty on the derivative corresponds to to statistical uncertainty on the data points, the second uncertainty corresponds to systematic uncertainty on the data points assuming they are fully correlated and the third uncertainty corresponds to the systematic uncertainty on the data points assuming they are fully uncorrelated. Also shown are the significances of the derivative values from zero

$\sqrt{s_{\rm NN}}$ (GeV)	Derivative of polynomial ($\kappa\sigma^2$)	Sig.	Derivative of polynomial ($S\sigma$)	Sig.
7.7	–0.341$\pm$ 0.142 $\pm$ 0.031 $\pm$ 0.079	2.1	0.0071 $\pm$ 0.0214 $\pm$0.0054 $\pm$ 0.0111	0.3
11.5	–0.212 $\pm$ 0.087 $\pm$ 0.022 $\pm$ 0.045	2.2	–0.0094 $\pm$ 0.0088 $\pm$0.0029 $\pm$ 0.0044	1.0
14.5	–0.133 $\pm$ 0.055 $\pm$ 0.016 $\pm$ 0.026	2.2	–0.0161$\pm$0.004$\pm$ 0.0014 $\pm$ 0.0024	3.5
19.6	–0.039 $\pm$ 0.023 $\pm$ 0.009 $\pm$ 0.013	1.5	–0.0189 $\pm$0.0031 $\pm$0.0001 $\pm$0.002	5.1
27	0.026 $\pm$ 0.019 $\pm$ 0.002 $\pm$ 0.014	1.1	–0.0135$\pm$ 0.0017$\pm$ 0.0004 $\pm$ 0.00125	6.4
39	0.0203$\pm$ 0.0107 $\pm$ 0.001 $\pm$ 0.01	1.4	–0.0052$\pm$0.00221$\pm$0.0005 $\pm$ 0.0017	1.9
54.4	–0.008 $\pm$ 0.018 $\pm$ 0.001 $\pm$ 0.011	0.4	–0.0072$\pm$0.0026$\pm$0.0001$\pm$ 0.0024	2.0
62.4	0.05 $\pm$0.058 $\pm$ 0.002 $\pm$ 0.047	0.7	0.0059 $\pm$0.007$\pm$ 0.0025$\pm$ 0.0062	0.6

This results in a new collision energy dependence of $\kappa\sigma^2$ and $S\sigma$. This new set of data is then fitted to the same order polynomial function as the default case and the derivative is obtained at each collision energy. This process is repeated until the width of the distribution of derivative values at each collision energy converges. The width of this distribution is taken as the uncertainty on the derivative value. For obtaining the fully correlated systematic uncertainty on the derivative value, all the $\kappa\sigma^2$ or $S\sigma$ data points are shifted up or down by the systematic uncertainties together. Then the resultant collision energy dependence of $\kappa\sigma^2$ or $S\sigma$ is fitted by the same order polynomial function as the default case and derivative values obtained. The difference in the derivative values from the default values is taken as the correlated systematic uncertainty on the derivative values. Also shown in the Table 2 are the significance values for the derivative to be non-zero at each $\sqrt{s_{\rm NN}}$, calculated using the statistical and the uncorrelated systematic uncertainties added in quadrature.

Various ansatz related to the fitting procedure have been checked to determine the robustness of the sign change of the derivative values. These includes fitting the data to various orders of polynomial function and varying the fitting range. Further, as suggested in Ref. [16] the $\kappa\sigma^2$ was plotted as a function of M/σ^2 to study the sign change of the derivative values. The values of the derivatives of the fourth order polynomial functions for $\kappa\sigma^2$ versus M/σ^2 are given in Table 3. The conclusions of such studies qualitatively remain the same as presented in the current work. The significance of the non-monotonic variation of $\kappa\sigma^2$ with M/σ^2 was found to be 3.1σ.

As a cross check, we have estimated the uncorrelated systematic uncertainties on the derivative values by assuming the probability distribution for the uncertainties to be a uniform distribu-

Table 3: Values of the derivative of fourth order polynomial that describes the $\kappa\sigma^2$ versus M/σ^2 (C_1/C_2). The first uncertainty on the derivative corresponds to to statistical uncertainty on the data points, the second uncertainty corresponds to systematic uncertainty on the data points assuming they are fully correlated and the third uncertainty corresponds to the systematic uncertainty on the data points assuming they are fully uncorrelated.

$\sqrt{s_{\rm NN}}$ (GeV)	C_1/C_2	Derivative of polynomial ($\kappa\sigma^2$)	Sig.
7.7	1.067	14.967 $\pm$ 13.12 $\pm$ 1.749 $\pm$ 6.965	1.0
11.5	1.035	12.17 $\pm$ 9.109 $\pm$ 1.47 $\pm$ 4.625	1.2
14.5	0.979	7.833 $\pm$ 4.114 $\pm$ 1.034 $\pm$ 1.869	1.7
19.6	0.901	3.176 $\pm$ 1.953 $\pm$ 0.56 $\pm$ 1.315	1.3
27	0.77	–1.365 $\pm$ 1.64 $\pm$ 0.072 $\pm$ 0.9973	0.7
39	0.597	–1.878$\pm$ 1.605 $\pm$ 0.055 $\pm$ 1.369	0.9
54.4	0.468	1.116 $\pm$ 3.216 $\pm$ 0.164 $\pm$ 2.029	0.3
62.4	0.425	2.634 $\pm$6.618 $\pm$ 0.285 $\pm$ 4.225	0.3

Table 4: Same as Table 2, except that the probability distribution for estimation of uncorrelated systematic uncertainties is assumed to be an uniform distribution.

$\sqrt{s_{\rm NN}}$ (GeV)	Derivative of polynomial ($\kappa\sigma^2$)	Sig.	Derivative of polynomial ($S\sigma$)	Sig.
7.7	–0.341$\pm$ 0.142 $\pm$ 0.031 $\pm$ 0.045	2.3	0.0071 $\pm$ 0.0214 $\pm$0.0054 $\pm$ 0.0064	0.3
11.5	–0.212 $\pm$ 0.087 $\pm$ 0.022 $\pm$ 0.026	2.3	–0.0094 $\pm$ 0.0088 $\pm$0.0029 $\pm$ 0.0026	1.0
14.5	–0.133 $\pm$ 0.055 $\pm$ 0.016 $\pm$ 0.015	2.3	–0.0161$\pm$0.004$\pm$ 0.0014 $\pm$ 0.0014	3.8
19.6	–0.039 $\pm$ 0.023 $\pm$ 0.009 $\pm$ 0.008	1.6	–0.0189 $\pm$0.0031 $\pm$0.0001 $\pm$0.0012	5.7
27	0.026 $\pm$ 0.019 $\pm$ 0.002 $\pm$ 0.008	1.3	–0.0135$\pm$ 0.0017$\pm$ 0.0004 $\pm$ 0.0007	7.3
39	0.0203$\pm$ 0.0107 $\pm$ 0.001 $\pm$ 0.006	1.7	–0.0052$\pm$0.00221$\pm$0.0005 $\pm$ 0.001	2.1
54.4	–0.008 $\pm$ 0.018 $\pm$ 0.001 $\pm$ 0.007	0.4	–0.0072$\pm$0.0026$\pm$0.0001$\pm$ 0.0014	2.4
62.4	0.05 $\pm$0.058 $\pm$ 0.002 $\pm$ 0.027	0.8	0.0059 $\pm$0.007$\pm$ 0.0025$\pm$ 0.00356	0.8

tion. The derivative value and the significance at each collision energy are shown in Table 4. The significance of the derivative values are increased compared to those shown in Table 2.

1. Llope, W. J. *et al.*, The TOFp / pVPD time-of-flight system for STAR, *Nucl. Instrum. Meth.* **A522**, 252 (2004).

2. Llope, W. J., Multigap RPCs in the STAR experiment at RHIC, *Nucl. Instrum. Meth.* **A661**, S110 (2012).

3. Anderson, M. *et al.*, The STAR time projection chamber: A unique tool for studying high multiplicity events at RHIC, *Nucl. Instrum. Meth.* **A499**, 659 (2003).

4. Esumi, S. and Nonaka, T., Reconstructing particle number distributions with convoluting volume fluctuations, *arXiv:2002.11253 [physics.data-an]*.

5. Nonaka, T., Recent Results and Methods on Higher Order and Off-diagonal Cumulants of Identified Net-particle Multiplicity Distributions in Au+Au Collisions at STAR, *Nucl. Phys.* **A982**, 863 (2019).

6. Nonaka, T., Kitazawa, M., and Esumi, S., More efficient formulas for efficiency correction of cumulants and effect of using averaged efficiency, *Phys. Rev.* **C95**, 064912 (2017).

7. Nonaka, T., Kitazawa, M., and Esumi, S., A general procedure for detector–response correction of higher order cumulants, *Nucl. Instrum. Meth.* **A906**, 10 (2018).

J. Adam[6], L. Adamczyk[2], J. R. Adams[39], J. K. Adkins[30], G. Agakishiev[28], M. M. Aggarwal[40], Z. Ahammed[59], I. Alekseev[3,35], D. M. Anderson[53], A. Aparin[28], E. C. Aschenauer[6], M. U. Ashraf[11], F. G. Atetalla[29], A. Attri[40], G. S. Averichev[28], V. Bairathi[22], K. Barish[10], A. Behera[51], R. Bellwied[20], A. Bhasin[27], J. Bielcik[14], J. Bielcikova[38], L. C. Bland[6], I. G. Bordyuzhin[3], J. D. Brandenburg[48,6], A. V. Brandin[35], J. Butterworth[44], H. Caines[62], M. Calderón de la Barca Sánchez[8], D. Cebra[8], I. Chakaberia[29,6], P. Chaloupka[14], B. K. Chan[9], F-H. Chang[37], Z. Chang[6], N. Chankova-Bunzarova[28], A. Chatterjee[11], D. Chen[10], J. H. Chen[18], X. Chen[47], Z. Chen[48], J. Cheng[55], M. Cherney[13], M. Chevalier[10], S. Choudhury[18], W. Christie[6], H. J. Crawford[7], M. Csanád[16], M. Daugherity[1], T. G. Dedovich[28], I. M. Deppner[19], A. A. Derevschikov[42], L. Didenko[6], X. Dong[31], J. L. Drachenberg[1], J. C. Dunlop[6], T. Edmonds[43], N. Elsey[61], J. Engelage[7], G. Eppley[44], R. Esha[51], S. Esumi[56], O. Evdokimov[12], A. Ewigleben[32], O. Eyser[6], R. Fatemi[30], S. Fazio[6], P. Federic[38], J. Fedorisin[28], C. J. Feng[37], Y. Feng[43], P. Filip[28], E. Finch[50], Y. Fisyak[6], A. Francisco[62], L. Fulek[2], C. A. Gagliardi[53], T. Galatyuk[15], F. Geurts[44], A. Gibson[58], K. Gopal[23], D. Grosnick[58], W. Guryn[6], A. I. Hamad[29], A. Hamed[5], J. W. Harris[62], S. He[11], W. He[18], X. He[26], S. Heppelmann[8], S. Heppelmann[41], N. Herrmann[19], E. Hoffman[20], L. Holub[14], Y. Hong[31], S. Horvat[62], Y. Hu[18], H. Z. Huang[9], S. L. Huang[51], T. Huang[37], X. Huang[55], T. J. Humanic[39], P. Huo[51], G. Igo[9], D. Isenhower[1], W. W. Jacobs[25], C. Jena[23], A. Jentsch[6], Y. JI[47], J. Jia[6,51], K. Jiang[47], S. Jowzaee[61], X. Ju[47], E. G. Judd[7], S. Kabana[29], M. L. Kabir[10], S. Kagamaster[32], D. Kalinkin[25], K. Kang[55], D. Kapukchyan[10], K. Kauder[6], H. W. Ke[6], D. Keane[29], A. Kechechyan[28], M. Kelsey[31], Y. V. Khyzhniak[35], D. P. Kikoła [60], C. Kim[10], B. Kimelman[8], D. Kincses[16], T. A. Kinghorn[8], I. Kisel[17], A. Kiselev[6], A. Kisiel[60], M. Kocan[14], L. Kochenda[35], L. K. Kosarzewski[14], L. Kramarik[14], P. Kravtsov[35], K. Krueger[4],

N. Kulathunga Mudiyanselage[20], L. Kumar[40], R. Kunnawalkam Elayavalli[61], J. H. Kwasizur[25], R. Lacey[51], S. Lan[11], J. M. Landgraf[6], J. Lauret[6], A. Lebedev[6], R. Lednicky[28], J. H. Lee[6], Y. H. Leung[31], C. Li[47], W. Li[44], W. Li[49], X. Li[47], Y. Li[55], Y. Liang[29], R. Licenik[38], T. Lin[53], Y. Lin[11], M. A. Lisa[39], F. Liu[11], H. Liu[25], P. Liu[51], P. Liu[49], T. Liu[62], X. Liu[39], Y. Liu[53], Z. Liu[47], T. Ljubicic[6], W. J. Llope[61], R. S. Longacre[6], N. S. Lukow[52], S. Luo[12], X. Luo[11], G. L. Ma[49], L. Ma[18], R. Ma[6], Y. G. Ma[49], N. Magdy[12], R. Majka[62], D. Mallick[36], S. Margetis[29], C. Markert[54], H. S. Matis[31], J. A. Mazer[45], N. G. Minaev[42], S. Mioduszewski[53], B. Mohanty[36], I. Mooney[61], Z. Moravcova[14], D. A. Morozov[42], M. Nagy[16], J. D. Nam[52], Md. Nasim[22], K. Nayak[11], D. Neff[9], J. M. Nelson[7], D. B. Nemes[62], M. Nie[48], G. Nigmatkulov[35], T. Niida[56], L. V. Nogach[42], T. Nonaka[11], G. Odyniec[31], A. Ogawa[6], S. Oh[62], V. A. Okorokov[35], B. S. Page[6], R. Pak[6], A. Pandav[36], Y. Panebratsev[28], B. Pawlik[2], D. Pawlowska[60], H. Pei[11], C. Perkins[7], L. Pinsky[20], R. L. Pintér[16], J. Pluta[60], J. Porter[31], M. Posik[52], N. K. Pruthi[40], M. Przybycien[2], J. Putschke[61], H. Qiu[26], A. Quintero[52], S. K. Radhakrishnan[29], S. Ramachandran[30], R. L. Ray[54], R. Reed[32], H. G. Ritter[31], J. B. Roberts[44], O. V. Rogachevskiy[28], J. L. Romero[8], L. Ruan[6], J. Rusnak[38], N. R. Sahoo[48], H. Sako[56], S. Salur[45], J. Sandweiss[62], S. Sato[56], W. B. Schmidke[6], N. Schmitz[33], B. R. Schweid[51], F. Seck[15], J. Seger[13], M. Sergeeva[9], R. Seto[10], P. Seyboth[33], N. Shah[24], E. Shahaliev[28], P. V. Shanmuganathan[6], M. Shao[47], F. Shen[48], W. Q. Shen[49], S. S. Shi[11], Q. Y. Shou[49], E. P. Sichtermann[31], R. Sikora[2], M. Simko[38], J. Singh[40], S. Singha[26], N. Smirnov[62], W. Solyst[25], P. Sorensen[6], H. M. Spinka[4], B. Srivastava[43], T. D. S. Stanislaus[58], M. Stefaniak[60], D. J. Stewart[62], M. Strikhanov[35], B. Stringfellow[43], A. A. P. Suaide[46], M. Sumbera[38], B. Summa[41], X. M. Sun[11], Y. Sun[47], Y. Sun[21], B. Surrow[52], D. N. Svirida[3], P. Szymanski[60], A. H. Tang[6], Z. Tang[47], A. Taranenko[35], T. Tarnowsky[34], J. H. Thomas[31], A. R. Timmins[20],

D. Tlusty[13], M. Tokarev[28], C. A. Tomkiel[32], S. Trentalange[9], R. E. Tribble[53], P. Tribedy[6], S. K. Tripathy[16], O. D. Tsai[9], Z. Tu[6], T. Ullrich[6], D. G. Underwood[4], I. Upsal[48,6], G. Van Buren[6], J. Vanek[38], A. N. Vasiliev[42], I. Vassiliev[17], F. Videbæk[6], S. Vokal[28], S. A. Voloshin[61], F. Wang[43], G. Wang[9], J. S. Wang[21], P. Wang[47], Y. Wang[11], Y. Wang[55], Z. Wang[48], J. C. Webb[6], P. C. Weidenkaff[19], L. Wen[9], G. D. Westfall[34], H. Wieman[31], S. W. Wissink[25], R. Witt[57], Y. Wu[10], Z. G. Xiao[55], G. Xie[31], W. Xie[43], H. Xu[21], N. Xu[31], Q. H. Xu[48], Y. F. Xu[49], Y. Xu[48], Z. Xu[6], Z. Xu[9], C. Yang[48], Q. Yang[48], S. Yang[6], Y. Yang[37], Z. Yang[11], Z. Ye[44], Z. Ye[12], L. Yi[48], K. Yip[6], H. Zbroszczyk[60], W. Zha[47], D. Zhang[11], S. Zhang[47], S. Zhang[49], X. P. Zhang[55], Y. Zhang[47], Y. Zhang[11], Z. J. Zhang[37], Z. Zhang[6], J. Zhao[43], C. Zhong[49], C. Zhou[49], X. Zhu[55], Z. Zhu[48], M. Zurek[31], M. Zyzak[17]

(STAR Collaboration)

[1]Abilene Christian University, Abilene, Texas 79699 [2]AGH University of Science and Technology, FPACS, Cracow 30-059, Poland [3]Alikhanov Institute for Theoretical and Experimental Physics NRC "Kurchatov Institute", Moscow 117218, Russia [4]Argonne National Laboratory, Argonne, Illinois 60439 [5]American University of Cairo, New Cairo 11835, New Cairo, Egypt [6]Brookhaven National Laboratory, Upton, New York 11973 [7]University of California, Berkeley, California 94720 [8]University of California, Davis, California 95616 [9]University of California, Los Angeles, California 90095 [10]University of California, Riverside, California 92521 [11]Central China Normal University, Wuhan, Hubei 430079 [12]University of Illinois at Chicago, Chicago, Illinois 60607 [13]Creighton University, Omaha, Nebraska 68178 [14]Czech Technical University in Prague, FNSPE, Prague 115 19, Czech Republic [15]Technische Universität Darmstadt, Darmstadt

64289, Germany [16]ELTE Eötvös Loránd University, Budapest, Hungary H-1117 [17]Frankfurt Institute for Advanced Studies FIAS, Frankfurt 60438, Germany [18]Fudan University, Shanghai, 200433 [19]University of Heidelberg, Heidelberg 69120, Germany [20]University of Houston, Houston, Texas 77204 [21]Huzhou University, Huzhou, Zhejiang 313000 [22]Indian Institute of Science Education and Research (IISER), Berhampur 760010 , India [23]Indian Institute of Science Education and Research (IISER) Tirupati, Tirupati 517507, India [24]Indian Institute Technology, Patna, Bihar 801106, India [25]Indiana University, Bloomington, Indiana 47408 [26]Institute of Modern Physics, Chinese Academy of Sciences, Lanzhou, Gansu 730000 [27]University of Jammu, Jammu 180001, India [28]Joint Institute for Nuclear Research, Dubna 141 980, Russia [29]Kent State University, Kent, Ohio 44242 [30]University of Kentucky, Lexington, Kentucky 40506-0055 [31]Lawrence Berkeley National Laboratory, Berkeley, California 94720 [32]Lehigh University, Bethlehem, Pennsylvania 18015 [33]Max-Planck-Institut für Physik, Munich 80805, Germany [34]Michigan State University, East Lansing, Michigan 48824 [35]National Research Nuclear University MEPhI, Moscow 115409, Russia [36]National Institute of Science Education and Research, HBNI, Jatni 752050, India [37]National Cheng Kung University, Tainan 70101 [38]Nuclear Physics Institute of the CAS, Rez 250 68, Czech Republic [39]Ohio State University, Columbus, Ohio 43210 [40]Panjab University, Chandigarh 160014, India [41]Pennsylvania State University, University Park, Pennsylvania 16802 [42]NRC "Kurchatov Institute", Institute of High Energy Physics, Protvino 142281, Russia [43]Purdue University, West Lafayette, Indiana 47907 [44]Rice University, Houston, Texas 77251 [45]Rutgers University, Piscataway, New Jersey 08854 [46]Universidade de São Paulo, São Paulo, Brazil 05314-970 [47]University of Science and Technology of China, Hefei, Anhui 230026 [48]Shandong University,

Qingdao, Shandong 266237 [49]Shanghai Institute of Applied Physics, Chinese Academy of Sciences, Shanghai 201800 [50]Southern Connecticut State University, New Haven, Connecticut 06515 [51]State University of New York, Stony Brook, New York 11794 [52]Temple University, Philadelphia, Pennsylvania 19122 [53]Texas A&M University, College Station, Texas 77843 [54]University of Texas, Austin, Texas 78712 [55]Tsinghua University, Beijing 100084 [56]University of Tsukuba, Tsukuba, Ibaraki 305-8571, Japan [57]United States Naval Academy, Annapolis, Maryland 21402 [58]Valparaiso University, Valparaiso, Indiana 46383 [59]Variable Energy Cyclotron Centre, Kolkata 700064, India [60]Warsaw University of Technology, Warsaw 00-661, Poland [61]Wayne State University, Detroit, Michigan 48201 [62]Yale University, New Haven, Connecticut 06520